Two-fluid modelling for poly-disperse bubbly flows in vertical pipes: Analysis of the impact of geometrical parameters and heat transfer

Nuclear Engineering and Technology 55 (2023) 1152–1166

Contents lists available at ScienceDirect

Nuclear Engineering and Technology

journal homepage: www.elsevier.com/locate/net

Original Article

Two-fluid modelling for poly-disperse bubbly flows in vertical pipes: Analysis of the impact of geometrical parameters and heat transfer

Andrea Allio [a], Antonio Buffo [b], Daniele Marchisio [b], Laura Savoldi [a, *]

[a] Politecnico di Torino, Dipartimento Energia "Galileo Ferraris", Corso Duca degli Abruzzi 24, 10129, Torino, Italy
[b] Politecnico di Torino, Dipartimento di Scienza Applicata e Tecnologia, Corso Duca degli Abruzzi 24, 10129, Torino, Italy

ARTICLE INFO

Article history:
Received 30 March 2022
Received in revised form
24 September 2022
Accepted 5 December 2022
Available online 10 December 2022

Keywords:
Bubbly flow
Computational fluid dynamics
Multiphase flows
Two-fluid model
Vertical pipe
Interfacial closures
Poly-disperse

ABSTRACT

The bubbly flow of air or steam in subcooled water are investigated here in several test cases, characterized by different pipe sizes, bubble dimensions and flow rates, by means of CFD using a Eulerian-Eulerian approach. The performance of models that differ for the turbulence closure in the continuous phase, as well as for the description of the lift force on the dispersed phase, are compared in detail. When air is considered, the space of the experimental parameters leading to a reasonable performance for the selected models are identified and discussed, while the issues left in the modelling of the concurrent condensation are highlighted for the cases where steam is used.

1. Introduction

Bubbly flows can be found in a wide range of multiphase flow engineering applications and industries, including nuclear and chemical engineering. The use of computational fluid dynamics (CFD) to solve and analyze problems involving multiphase flows is growing in popularity. This technique provides a numerical tool that can account for a variety of local phenomena at the bubble scale that affect the macroscopic behaviour of the flow. The ever-increasing availability of computational resources has aided in the development of interface-capturing methods. Gas–liquid interfaces can be resolved using such techniques, and closure models for the interactions between phases are not required. However, due to the huge computational effort required, this type of approach can currently be used only in very simple systems with a small number of bubbles [1]. A feasible solution for real-world industrial problems is to use an averaged description provided by the Eulerian-Eulerian Two-Fluid models in which physical processes are not solved at the bubble scale. In fact, a set of conservation equations is solved for each averaged phase, and closure relations are required to couple the phases in terms of mass, momentum, and energy exchanges. The closure relations representing interphase momentum transfer, known as interfacial forces, are essential, and much research effort has gone into developing more and more accurate forms for them. Drag, lift, turbulent dispersion, and wall lubrication are the most common interfacial forces [2]. In non-adiabatic cases, when there is a temperature difference between the phases, also interphase energy exchange occurs and other closure relations are required to describe this phenomenon. All those elements are interconnected and cannot be considered separately. Bubble interfacial forces and interphase mass transfer closures are normally a function of the bubble size, and bubbly flows are typically polydisperse. This type of flow is characterized by significant particle size changes caused by collisions, which cause bubble coalescence, and shear forces, which cause breakup into smaller ones [3]. Energy transfer between phases also has an important impact on the change in the bubble size, due to the occurrence of condensation and evaporation phenomena.

In recent years, some researchers have proposed CFD baseline models that can cover a wide range of conditions without requiring any adjustments. Researchers at the Helmholtz-Zentrum Dresden-Rosendorf (HZDR) have developed a general strategy that includes bubble force closures, bubble-induced turbulence, and bubble

* Corresponding author.
E-mail address: laura.savoldi@polito.it (L. Savoldi).

https://doi.org/10.1016/j.net.2022.12.005

coalescence and breakup for polydisperse flows [3]. A large database of experimental cases has been used to validate the model. Some cases involving steam-water systems that require a treatment for steam condensation have also been investigated. Two of those steam-water cases were considered in this paper [4]. These concepts were also followed by researchers at the University of Leeds when developing a CFD baseline model. Their model does not describe the bubbles as polydisperse and it has been validated by using experimental cases including mostly monodisperse flows, covering a wide range of operational and geometric conditions. Not only upward flows in cylindrical pipes were analysed, but also downward flows and noncircular tubes [5,6].

It should be noted, however, that the development of the above-mentioned baseline models is often carried out considering different datasets for modeling validation and different CFD codes as modeling tools. While the models are proven to give good predictions for the investigated datasets for a specific code, nothing certain can be said about their applicability to other test cases, or when the same model is implemented on a different CFD code, since each code may have its own different numerical treatment of the equations. These aspects unfortunately undermine the general validity of the approach and makes modeling new systems difficult. Moreover, connected to this aspect there is also the complexity of those models, that it is caused by the multiplicity of the sub-models, the relative importance of which is often unknown, and the derivation of which may be the result of arbitrary assumptions. One possible approach to overcome these issues is to run numerous simulations considering a wide range of models and test cases, to identify which is the simplest model that gives the best predictions on the largest set of tests cases and operating conditions.

In the present work, the Eulerian-Eulerian Two-Fluid modelling strategy was investigated for the simulation of vertical pipe bubbly flows, and three different proposed models were compared with the baseline models in a wide range of experimental cases. The CFD code used in this work is commercial software STAR-CCM+ [7]. The aim of the work is to analyze different operating conditions and different diameters of vertical pipes, staying within the bubbly flow regime, and trying to use the simplest possible closure models to obtain a good prediction for the largest set of experimental data considered. A polydisperse treatment based on the $S-$ Gamma method of moments and an interphase heat and mass transfer modelling for non-adiabatic conditions are used, with the final goal of properly describing the behaviour of condensing steam-water systems. A schematic representation of the experimental cases investigated in this work is reported in Fig. 1.

After introducing the governing equations and all the closure relations which are used to describe the bubbly flows in Section 2, the computational details of the CFD model and the adopted tool are provided in Section 3. Simulation results and the comparison with experimental data, and model results provided by other authors are discussed in Section 4. A brief conclusion with a prediction of the future steps is reported in Section 5.

2. Governing equations

The Eulerian-Eulerian two-fluid model is adopted, where water is considered as continuous phase and air or steam as dispersed phase [8]. A set of conservation equations for mass and momentum is solved for each phase [7]:

$$\frac{\partial}{\partial t}(\alpha_i\rho_i) + \nabla \bullet (\alpha_i\rho_i\boldsymbol{v}_i) = \sum_{j\neq i}(m_{ij} - m_{ji}) \qquad 1$$

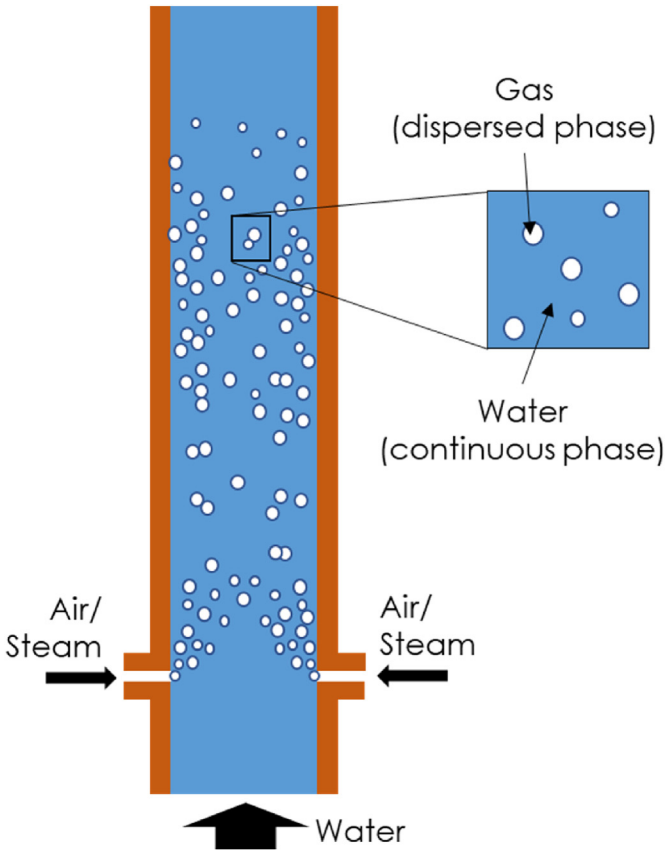

Fig. 1. Schematic of the experimental case-study analysed in the present work: bubbly flow in vertical pipes, with indications of the continuous and dispersed phases.

$$\frac{\partial}{\partial t}(\alpha_i\rho_i\boldsymbol{v}_i) + \nabla \bullet (\alpha_i\rho_i\boldsymbol{v}_i\boldsymbol{v}_i) = -\alpha_i\nabla p + \alpha_i\rho_i\boldsymbol{g} + \nabla \bullet \left(\alpha_i\left(\boldsymbol{T}_i + \boldsymbol{T}_i^t\right)\right) + \boldsymbol{M}_i + \sum_{j\neq i}\left(m_{ij}\boldsymbol{v}_j - m_{ji}\boldsymbol{v}_i\right). \qquad 2$$

The continuity and momentum equations are sufficient to describe the adiabatic cases, i.e., all the air-water flow cases here investigated. To simulate the cases which involve steam as dispersed phase, the energy conservation equation (Eq. (3)) is also needed:

$$\frac{\partial}{\partial t}(\alpha_i\rho_i E_i) + \nabla \bullet (\alpha_i\rho_i H_i\boldsymbol{v}_i) + \nabla \bullet (\alpha_i p) = \nabla \bullet \left(\alpha_i k_{eff,i}\nabla T_i\right) + \nabla \bullet (\boldsymbol{T}_i \bullet \boldsymbol{v}_i) + \sum_{j\neq i} Q_{ij} + \sum_{(ij)} Q_i^{(ij)} + \sum_{j\neq i}(m_{ij} - m_{ji})h_i(T_{ij}), \qquad 3$$

where $k_{eff,i} = k_i + (\mu_{t,i}\, C_{p,i})/\sigma_{t,i}$. In the above equations the subscript i represents the generic phase, continuous or dispersed. The term $\boldsymbol{M}_i$ in Eq. (2) is the interfacial momentum transfer between the phases per unit volume source, it is defined by the closure relations that model the interfacial forces. The terms m_{ij} and m_{ji} describe the mass transfer rate between the generic phases i and j. The terms Q_{ij} and $Q_i^{(ij)}$ in Eq. (3) represent respectively the sensible heat transfer between the phases due to the temperature difference between the phases and the latent heat transfer due to

condensation or evaporation. The last term of the equation refers to the exchange of energy between phases due to interfacial enthalpy evaluated at the temperature of the interface T_{ij}. When heat and mass are transferred through phase change, the heat transfer rates between each phase i, j and a phase pair interface (ij) satisfy the heat balance:

$$Q_i^{(ij)} + Q_j^{(ij)} + (m_{ij} - m_{ji})\Delta h_{ij}^{lat} = 0 \tag{4}$$

Where $\Delta h_{ij}^{lat} = h_j(T_{ij}) - h_i(T_{ij})$ is the phase change latent heat. All these terms of mass and heat transfer between the phases are different from zero only in the case of steam-water flow.

2.1. Interfacial forces

The closure relations of all the interfacial forces analysed in this work are described in the following section. In general, the interfacial momentum transfer can be defined as in Eq. (5):

$$\boldsymbol{M}_i = \sum_{j \neq i} \left(\boldsymbol{F}_{ij}^{D} + \boldsymbol{F}_{ij}^{L} + \boldsymbol{F}_{ij}^{TD} + \boldsymbol{F}_{ij}^{WL} + \boldsymbol{F}_{ij}^{VM} \right) \tag{5}$$

where $\boldsymbol{F}_{ij}^{D}$ is the drag force, $\boldsymbol{F}_{ij}^{L}$ the lift force, $\boldsymbol{F}_{ij}^{TD}$ the turbulent dispersion force and $\boldsymbol{F}_{ij}^{WL}$ the wall lubrication force.

The contribution of the virtual mass $\boldsymbol{F}_{ij}^{VM}$, which considers the influence of the fluid surrounding a bubble on its acceleration, is assumed negligible in this work since we are interested in the prediction of time-averaged profiles.

The drag force accounts for the friction effect generated by the motion of the gas bubbles into the liquid phase. It is expressed as:

$$\boldsymbol{F}_{ij}^{D} = \frac{3}{4\, d_b} C_D \rho_c \alpha_d |\boldsymbol{v}_r| \boldsymbol{v}_r \,, \tag{6}$$

where $\mathbf{v}_r = \mathbf{v}_d - \mathbf{v}_c$ is the relative velocity between the gas and the liquid phase, d_b is the bubble diameter and C_D is the drag coefficient. In this work, the model of Tomiyama for moderately contaminated state, corresponding to a partially immobile air-water interface is employed, where C_D is expressed in terms of the bubble Reynolds number Re ($\mathrm{Re} = (\rho_c |\boldsymbol{v}_r| d_b)/\mu_c$) and the Eötvös number Eo ($\mathrm{Eo} = (|\rho_c - \rho_d|\, g d_b^2)/\sigma$) [10] as:

$$C_D = max\left(min\left(\frac{24}{Re}\left(1 + 015\, Re^{0.687}\right), \frac{72}{Re} \right), \frac{8\, Eo}{3(Eo+4)} \right) . \tag{7}$$

The Eötvös number is a dimensionless number that relates the importance of gravitational forces over surface tension forces, μ_c is the dynamic viscosity of the continuous phase and σ is the surface tension between air/steam and water.

The lift force is a force perpendicular to the direction of the relative velocity and it is expressed as follows:

$$\boldsymbol{F}_{ij}^{L} = C_L \alpha_d \rho_c (\boldsymbol{v}_r \times (\nabla \times \boldsymbol{v}_c)) \,. \tag{8}$$

The value of the lift coefficient C_L is positive for small spherical bubbles and the bubbles are pushed in the direction of lower liquid velocity, so generally towards the wall. However, for large bubbles at high Re, the shape of bubbles changes from spherical to ellipsoidal. In these cases the force has opposite direction, so C_L can be negative [11]. Different models are used in this work to define the lift coefficient. For instance, Sugrue developed an approach based on the dimensionless Wobble number Wo [12]:

$$C_L = f(Wo) f(\alpha_d) \,, \tag{9}$$

where $f(\mathrm{Wo}) = \min(0.03,\ 5.0404 - 5.0781\ \mathrm{Wo}^{0.0108})$, $\mathrm{Wo} = \mathrm{Eo}\frac{k_c}{|\boldsymbol{v}_r|^2}$ and $f(\alpha_d) = 1.0155 - 0.0154\, e^{8.0506\ \alpha_d}$. According to the definition given in the work of Sugrue et al. [20], the Wobble number is essentially a modified Eötvös number that considers also the unsteady behaviour of the bubbles in turbulent flow conditions. The parameter k_c appearing in the Wo definition is in fact the turbulent kinetic energy of the continuous phase. The correlation in Eq. (9) has been adopted by Shiea and co-workers in Ref. [2] providing good results.

Tomiyama et al. proposed a correlation developed through the experimental examination of the trajectories of a single bubble in high-viscosity liquids [11], which reads as follows:

$$C_L = \begin{cases} 0.288\, tanh(0.121\, max(Re, 7.374)) & Eo_d < 4 \\ 0.00105\, Eo_d^3 - 0.0159\, Eo_d^2 - 0.0204\, Eo_d + 0.474 & 4 \leq Eo_d \leq 10 \\ -0.27 & 10 < Eo_d \end{cases} , \tag{10}$$

where Eo_d is the modified Eötvös number, based on the maximum horizontal dimension of a bubble ($\mathrm{Eo}_d = \mathrm{E_o}(1 + 0.163\ \mathrm{Eo}^{0.757})^{2/3}$) [13]. The lift force defined in Eq. (8) generally has a maximum at the wall, due to a non-null lift coefficient and a large velocity gradient. This results in an unphysical accumulation of bubbles near the wall, that in reality is hindered by steric effects. In order to avoid this unphysical bubble accumulation at the wall, the effect of the lift force can be reduced by using a damping factor, as suggested by Shaver and Podowsky [14]:

$$C_L = \begin{cases} 0 & y/d_b < 0.5 \\ C_L \left(3\left(\frac{2y}{d_b} - 1\right)^2 - 2\left(\frac{2y}{d_b} - 1\right)^3 \right) & 0.5 \leq \frac{y}{d_b} \leq 1 \\ C_{L,0} & y/d_b > 1 \end{cases} , \tag{11}$$

where $C_{L,0}$ is the nominal lift coefficient and y the wall distance of the gas phase from the wall. Colombo et al. suggested to use a constant value for the lift coefficient $C_L = 0.1$, used in conjunction with the damping factor defined by Shawer and Podowsky in Eq. (11) [5].

The turbulent dispersion force accounts for the effect of the turbulent fluctuations of liquid velocity on the bubbles. This force transports gas bubbles from regions with a high gas volume fraction to regions with a low gas volume fraction. In this work, the model proposed by Burns er al. is employed [15]:

$$\boldsymbol{F}_{ij}^{TD} = \frac{3}{4} C_D \frac{\alpha_d \rho_c}{d_b} |\boldsymbol{v}_r| \frac{\nu_c^t}{\sigma_\alpha} \left(\frac{1}{\alpha_d} + \frac{1}{1 - \alpha_d} \right) \nabla \alpha_d \,, \tag{12}$$

where ν_c^t is the turbulent kinematic viscosity of the continuous phase, and σ_α is the turbulent Prandtl number for the volume fraction of the dispersed phase. In this work, a constant value of $\sigma_\alpha = 0.9$ is imposed [2].

The wall lubrication is a fictitious force per unit volume usually added in the closure relations in order to prevent the unphysical accumulation of bubbles close to the walls. The use of this force mimics the experimental evidence that bubbles near the wall tend to rise while remaining at a certain distance from the wall. The general expression of the wall lubrication force, proposed by Antal et al. is reported in the following equation [16]:

$$\boldsymbol{F}_{ij}^{WL} = -C_{WL}\frac{\alpha_d \rho_c}{d_b}|\boldsymbol{v}_{r,\parallel}|^2 \boldsymbol{n}_w \,. \tag{13}$$

The term $\boldsymbol{v}_{r,\parallel}$ is the component of the relative velocity parallel to the wall, $\boldsymbol{n}_w = [\boldsymbol{v}_r - (\boldsymbol{v}_r \cdot \boldsymbol{n})\,\boldsymbol{n}]$ is the unit normal at the nearest point of the wall, C_{WL} is the wall lubrication coefficient. The expression of C_{WL} used in this work is:

$$C_{WL} = max\left(-0.005 + 0.05\frac{d_b}{y}, 0\right) \tag{14}$$

and it depends on the wall distance from the cell center y [17].

2.2. Poly-disperse modelling

The mass and momentum transport equations must be linked with a population balance equation to account for the spatial and time evolution of the bubble size distribution of the dispersed phase [9]:

$$\frac{\partial n(d_b)}{\partial t} + \nabla \bullet (\boldsymbol{v}\, n(d_b)) = B - D \tag{15}$$

The variable $n(d_b)$ is the bubble size distribution (BSD), which corresponds to the number of bubbles per unit volume with size ranging from d_b to $d_b + d(d_b)$. In this context, usually bubbles are considered spherical and d_b is the equivalent diameter of a sphere with volume identical to that of the bubble. B and D are the source and sinks terms due to breakup and coalescence of bubbles.

To solve Eq. (15), the method of moments S-gamma is used, which calculates the zero-th and second order moments of BSD, $n(d_b)$, representing the number of bubbles whose diameter range between d_b and $d_b + d(d_b)$. Bubbles change size as they interact with each other due to breakup, coalescence, or due to growth/shrink phenomena such as mass transfer or condensation. The S-Gamma model relies on the assumption that the BSD follows a predefined log-normal probability density function $P(d_b)$ [22,23], as it can be seen in the following expression:

$$n(d_b) = nP(d_b) = \frac{n}{d_b \sigma_{d_b}\sqrt{2\pi}} exp\left(\frac{(ln(d_b) - \mu_{d_b})^2}{2\,\sigma_{d_b}^2}\right) \tag{16}$$

The quantities σ_{d_b} and μ_{d_b} represents the mean logarithmic and the standard deviation of BSD. The S-Gamma model defines S_γ, a quantity related to the moment of the particle size distribution M_γ, as reported in the following expression:

$$S_\gamma = n\,M_\gamma = n\int_0^\infty d_b^\gamma\, P(d_b)\, dd_b, \tag{17}$$

where γ is the order of the moment and n is the number of bubbles per unit volume (the Zeroth order moment). One transport equation is solved for each S_γ according to the definition [18] in Eq. (18):

$$\frac{\partial S_\gamma}{\partial t} + \nabla \cdot (S_\gamma \boldsymbol{v}_d) = s_{br} + s_{cl}, \tag{18}$$

where s_{br} and s_{cl} are the source terms that represents the effect of bubble breakup and coalescence. With the zero-th moment S_0, the second moment S_2, and the volume fraction of gas α_d, all other distribution parameters of Eq. (16) can be calculated assuming a log-normal distribution. The Sauter mean diameter d_{SM} can be calculated from S_2 (Eq. (17)) as:

$$d_{SM} = \frac{6\alpha_d}{\pi S_2} \tag{19}$$

In the interfacial forces and the interfacial heat transfer models (see section 2.3), the bubble size d_b is assumed to be equal to the Sauter mean diameter d_{SM}.

The source terms of the S_0 and S_2 equations are defined by sub-models that accounts for bubble coalescence and breakup. These sub-models are called kernels and quantify the frequency of coalescence and breakage events.

The breakup process can be divided into two parts: first the bubble is deformed by (turbulent) shear stresses and then depending on the extent of this deformation the bubble can break forming two or more fragments or relax to the original shape. Breakup is usually defined in terms of the breakage rate or frequency, and the fragments distribution or daughter distribution function. The source term for breakup s_{br} in S_0 and S_2 equations is defined as [18]:

$$s_{br} = \int_{d_{low}}^{d_{high}} nP(d_b)\frac{N_f(d_b)^{\frac{3-\gamma}{3}} - 1}{\tau_{br}(d_b)} d_b^\gamma\, dd_b, \tag{20}$$

where n is the number of bubbles per unit volume, $P(d)$ is the probability density function of bubble size, $N_f(d)$ is the number of fragments generated after a breakup event of a bubble of diameter d, γ is the order of the moment (0 for S_0, 2 for S_2), τ_{br} is the breakup time. Since in this work only turbulent flows are considered, the breakup source term is given by the sum of the source terms for viscous and inertial breakups. For viscous breakup, the integral of Eq. (20) is computed in the range of bubble size $0 < d < L_k$. The critical diameter $d_{cr,visc}$ is defined as:

$$d_{cr,visc} = \frac{2\sigma\Omega_{cr}}{\mu_c\,\dot{\gamma}}, \tag{21}$$

where σ is the surface tension, μ_c the viscosity of the continuous phase, $\dot{\gamma}$ the local shear rate of the continuous phase, and Ω_{cr} the critical capillary number. The definition of Ω_{cr}, for turbulent flows, is reported in Ref. [19]. The Kolmogorov length scale L_k is defined as:

$$L_k = \left(\frac{\nu_c^3}{\varepsilon_c}\right)^{\frac{1}{4}}, \tag{22}$$

where ν_c and ε_c are the kinematic viscosity and turbulent kinetic energy dissipation rate of the continuous phase, respectively. For inertial breakup, the integral in Eq. (20) is solved for $d > L_k$. Only binary breakup events are considered ($N_f = 2$) and a symmetric Daughter Particles Size distribution, providing the information about the size distribution after a bubble breakup event, is assumed. The breakup rate K_{br}, defined as the reciprocal of the breakup time $1/\tau_{br}$, is calculated using the model proposed by Tsouris and Tavlarides [20,21]:

$$K_{br} = C_g\frac{(\varepsilon_c d_b)^{\frac{1}{3}}}{d_b} exp\left(-K_1\frac{We_{cr}}{We}\right), \tag{23}$$

where C_g ($= 2$) and K_1 are calibration constants, We is the Weber number, and We_{cr} is the critical Weber number, which is assumed constant and equal to 0.31, as suggested by Yao and Morel [22]. The Weber number We, measuring the relative importance of the fluid inertia with respect to its surface tension, is defined here as [23]:

$$We = \frac{\rho_c (\varepsilon_c d_b)^{\frac{2}{3}} d_b}{\sigma} \left(\frac{\rho_d}{\rho_c}\right)^{\frac{1}{3}}, \tag{24}$$

where ρ_d is the density of the dispersed phase.

Also coalescence usually occurs in two steps. Initially the two-colliding steam/air bubbles are brought into close proximity by turbulent velocity fluctuations, then the film of water in between them needs to be drained, in order to result into a successful coalescence event. The coalescence kernel contains therefore two terms: the collision rate and the coalescence efficiency. The source term for coalescence s_{cl}, in S_0 and S_2 equations, is defined as [18]:

$$\begin{aligned} s_{cl} = & \frac{1}{2} \int_0^\infty \int_0^\infty K_{coll} P_{cl} n^2 P(d_i) P(d_j) \left(d_i^3 + d_j^3\right)^{\frac{\gamma}{3}} dd_i dd_j \\ & - \int_0^\infty d_i^\gamma n P(d_i) \int_0^\infty n P(d_j) K_{coll} P_{cl} dd_j dd_i, \end{aligned} \tag{25}$$

where γ is the order of the moment (0 for S_0, 2 for S_2), K_{coll} is the collision rate, P_{cl} is the probability that a collision produces coalescence. The collision rate K_{coll}, defined as number of collisions per unit volume per unit time, is computed using the correlations for turbulent flows proposed by Zaichik et al. [24] for bubbles suspended in turbulent liquid assuming bubble sizes in the inertial subrange:

$$K_{coll} = \left(\frac{2\pi}{15}\right)^{1/2} v_r \left(\frac{2\, d_i d_j}{d_i + d_j}\right)^2 \left(\frac{6\alpha_d}{\pi \left(\frac{2\, d_i d_j}{d_i + d_j}\right)^3}\right)^2 \tag{26}$$

K_{coll} is calculated as the probability of collisions of two spheres with diameters d_i and d_j moving with random relative velocity $v_r = \left(\varepsilon_c \frac{d_i + d_j}{2}\right)^{1/3}$, where ε_c is the turbulent dissipation rate of the liquid phase. The probability that a collision causes coalescence P_{cl}, also called coalescence efficiency, is calculated using the approach proposed by Luo [25]. The coalescence occurs when the contact time $t_{contact}$ overcomes the time $t_{rupture}$ required to drain the liquid film between two bubbles:

$$P_{cl} = exp\left(-\frac{t_{rupture}}{t_{contact}}\right), \tag{27}$$

The contact time $t_{contact}$ is defined considering coalescence in case of partial-mobile liquid-gas interfaces. The rupture time $t_{rupture}$ is defined using the parallel film concept described in Ref. [25]. The resulting equation for the coalescence efficiency is written as:

$$P_{cl} = exp\left(-K_2 \frac{\left(0.75\left(1 + \xi_{ij}^2\right)\left(1 + \xi_{ij}^3\right)\right)^{\frac{1}{2}}}{\left(\frac{\rho_d}{\rho_c} + C_{VM}\right)^{\frac{1}{2}} \left(1 + \xi_{ij}\right)^3} We_{ij}^{1/2}\right), \tag{28}$$

where K_2 is a calibration constant (= 0.698), C_{VM} is the virtual mass coefficient, taken equal to 0.5, $\xi_{ij} = d_i/d_j$ is the ratio between the diameter of two bubbles, We_{ij} is the Weber number defined now as:

$$We_{ij} = \frac{\rho_c 2\varepsilon_c^{2/3} \left(\frac{2\, d_i d_j}{d_i + d_j}\right)^{5/3}}{\sigma} \tag{29}$$

The integrals in Eqs. (20) and (25) are solved numerically by a discrete quadrature with 8 log-normally-distributed quadrature points.

2.3. Interfacial heat transfer

The rate of mass transfer between phases, defined as $(m_{ij} - m_{ji})$ in Eq. (3), is determined by the rate of heat transfer from the liquid and vapor to the saturated interface between these two phases. Because the steam is injected at saturation temperature in the cases studied, the rate of mass transfer between the bubble interface and the liquid can be defined as:

$$m_{ij} - m_{ji} = \frac{Q^{(ij)}}{\Delta h_{ij}^{lat}} = \frac{h_c (T_{sat} - T_c) a_{ij}}{\Delta h_{ij}^{lat}}. \tag{30}$$

The terms $Q^{(ij)}$ and Δh_{ij}^{lat} are the interphase latent heat transfer and the latent heat, respectively, h_c is the heat transfer coefficient between the interface of the bubbles and the liquid phase, T_{sat} and T_c are the saturation temperature and the temperature of the liquid. Assuming that bubbles have a spherical shape, the interaction area density a_{ij} is defined as:

$$a_{ij} = \pi S_2, \tag{31}$$

where S_2 is the second order moment computed by the polydisperse model.

The heat transfer coefficient h_c is computed using a correlation proposed by Tomiyama [26]:

$$h_c = \frac{Nu_c\, k_c}{d_b} = \frac{k_c}{d_b}\left(2 + 0.15\, Re^{0.8}\, Pr_c^{0.5}\right). \tag{32}$$

The Reynolds number Re is defined using the relative velocity between the phases and the bubble diameter. Pr_c is the Prandtl number defined for the liquid phase. This correlation was obtained by the experimental observation of the dissolution of CO_2 in water and applied by analogy.

2.4. Turbulence

While the disperse phase was considered in laminar conditions, the continuous phase was modelled using a turbulence closure in the present work, which is necessary to compute the turbulent stress tensor $\boldsymbol{T}_i^t$ in Eq. (2). Two different Reynolds-Averaged Navier Stokes (RANS) models was adopted: a two-equations standard $k - \varepsilon$ model and an ellipting-blending Reynolds Stress Model (EB-RSM).

The standard $k - \varepsilon$ turbulence model is a two-equation model that determine the turbulent eddy viscosity solving equations for turbulent kinetic energy k and turbulent dissipation rate ε. This model is applied together with a High-Reynolds wall treatment which uses standard wall functions at the wall [27].

Reynolds Stress models, also known as second-moment closure models, solve the governing transport equations to directly calculate the components of the Reynolds stress tensor. Because the transport equations for the Reynolds stresses naturally account for the effects of turbulence anisotropy and streamline curvature, RSM have the potential to predict complex flows more accurately than eddy viscosity models. The elliptic blending RSM (EB-RSM) model is a variant of the Quadratic Pressure-Strain RSM model which uses

Table 1
Summary of the models and their closure relations.

Closures	Model A	Model B	Model C
Drag force	Tomiyama (Eq. (7))	Tomiyama (Eq. (7))	Tomiyama (Eq. (7))
Lift Force	Sugrue (Eq. (9))	Tomiyama (Eq. (10)) + Shaver Podowksy correction (Eq. (11))	Constant $C_L = 0.10$ + Shaver Podowksy correction (Eq. (11))
Turbulent dispersion force	Burns (Eq. (12))	Burns (Eq. (12))	Burns (Eq. (12))
Wall lubrication force	Antal (Eq. (13))	Antal (Eq. (13))	Antal (Eq. (13))
Interphase mass transfer model	Tomiyama (Eq. (10))	–	–
Turbulence model (continuous phase)	Standard $k-\varepsilon$	EB-RSM	EB-RSM
Wall treatment (continuous phase)	Wall functions	Near-wall Low-Re	Near-wall Low-Re
Turbulence model (dispersed phase)	Laminar	Laminar	Laminar
Population balance	S-gamma	S-gamma	S-gamma

low-Reynolds wall treatment [28].

The models presented in this work do not include a treatment for the bubble-induced turbulence. Although it is known that the turbulence of the liquid phase is influenced by the motion of the bubbles, no unanimous agreement on the methods used to model this phenomenon has yet been reached and for this reason we decided to neglect this aspect [2].

2.5. Summary of the models

Three different models were developed to simulate all the experimental cases considered in this work. It should be remarked that the flow is considered poly-disperse in all cases, so all models include the population balance model solved by the S-gamma method described in Section 2.2. Therefore, the solution of the population balance can influence the fluid dynamics, since the bubble mean Sauter diameter is calculated in every point of the computational domain, and it is used to evaluate locally the interfacial forces acting between the bubbles and the surrounding continuous phase.

The features of each model are summarized in Table 1. Model A was obtained using the interfacial force closures suggested by Shiea et al. [2], except for the wall lubrication, for which the relation of Antal was used in place of the Hosokawa model [29]. Model B is derived from model A, but with the change of two closure relations, and namely the lift force and the turbulence modelling. The EB-RSM with a near-wall treatment, and the Lift coefficient proposed by Tomiyama were in fact adopted. Model C is a variant of model B, where the lift coefficient was imposed constant and equal to 0.1. This modification was performed as in analogy with the work of Shiea et al. [2], in order to find a constant lift coefficient that on the average gives the best predictions in terms of volume fraction profiles for the majority of the test cases investigated. This at least partially decouples the fluid dynamics from the local bubble size predicted by the population balance, simplifying the phase coupling issue related to the well-known lift coefficient sign inversion [11]. With this aim, in Model C the Tomiyama lift relation was replaced by a constant lift coefficient $C_L = 0.1$, as suggested by Colombo et al. in similar experimental setup [5].

3. Test cases and numerical details

Numerous experimental datasets have been considered for this works. All of them consist of vertical tubes of different diameters and heights in which water and air, or steam, bubbles flow upward. Table 2 summarizes the experimental datasets and the values of the main quantities adopted in the simulations. Beyer et al. [30] (cases 008, 028, 042, 063, 072) studied air-water upward flows in a pipe in

Table 2
– *Experimental database. The main characteristics of each dataset are reported: tube diameter (D_{pipe}), superficial velocities of continuous and dispersed phases (j_c and j_d), average volume fraction of gas (α_d), average bubble size (d_b).*

Case n.	D_{pipe} (m)	j_d (m/s)	j_c (m/s)	α_d	d_b (mm)	Ref.
008	195	0.0025	1.017	0.0025	4.24	[30]
063	195	0.0062	0.405	0.0151	5.34	
042	195	0.0062	0.405	0.0151	5.34	
072	195	0.0062	0.405	0.0151	5.34	
028	195	0.0062	0.405	0.0151	5.34	
118–1	195	0.2190	1.017	0.1770	12.00	[4]
118–6	195	0.2190	1.017	0.1770	8.00	
H11	25	0.0180	0.500	0.0250	3.21	[31]
H12	25	0.0250	0.500	0.0410	4.25	
H21	25	0.0200	1.000	0.0150	3.52	
H22	25	0.0360	1.000	0.0320	3.66	
LB17	38	0.1120	0.753	0.1091	3.07	[32]
LB30	38	0.0670	1.087	0.0470	2.39	
LB31	38	0.1120	1.087	0.0737	2.92	
L11A	57.2	0.1200	0.500	0.1520	2.94	[33]
L21C	57.2	0.1300	1.000	0.0960	4.22	
L21B	57.2	0.1200	0.500	0.1520	2.94	
L22A	57.2	0.2200	1.000	0.1570	3.89	

the TOPFLOW facility at HZDR. The pipe has an inner diameter of 195.3 mm, a height of 8 m and the experiments were performed at a flow pressure of 2.5 bar and temperature of 30 °C. Air was injected in the water flow through a ring of holes drilled in the wall of the pipe. The outputs of the experiment are the radial profiles of volume fraction, gas velocity, and bubble size distribution. They are measured using a wire mesh sensor located at the top of the tube. To analyze the profiles at different distance from the air inlet, measurements were repeated varying the position of the injection ring. Liao et al. [4] (cases 118−1, 118−6) analysed the poly-disperse modelling of a steam-water upward flow in the TOPFLOW test section, already described before. Steam was injected at saturation temperature, instead water enters in the pipe in sub-cooled conditions. In the case 118−1 the injection pressure is 1 MPa and the degree of water subcooling is 3.9 °C. In the case 118−6 the injection pressure is 4 MPa and the degree of water subcooling is 5.0 °C.

Hosokawa et al. [31] (cases H11, H12, H21, H22) studied an air-water upward flow in a tube with an inner diameter of 25 mm and a height of 2 m. Experiments are conducted at atmospheric pressure and temperature. The outputs of the experiments are the radial profiles of the volume fraction of gas, average bubble diameter, liquid and gas velocity. These quantities are measured at a distance from the air injection point equal to $L/D = 68$. Liu and Bankoff [32] (cases LB17, LB30, LB31) analysed an air-water upward bubbly flow in a tube of inner diameter equal to 38 mm. The measurements of radial profiles of volume fraction, gas and liquid velocity, and bubble diameter were taken at a distance $L/D = 36$ from the injection point. Liu [33] (cases L11A, L21C, L21B, L22A) investigated an upward air-water flow in a tube of inner diameter of 57.2 mm. The experiments were performed at ambient pressure and at a temperature of 26 °C. The radial profiles of volume fraction of gas, liquid velocity and the average bubble diameter were measured at a distance from the air injection of $L/D = 60$.

All the simulations were performed using the commercial software STAR-CCM+ [7]. Unsteady simulations using a first-order implicit scheme were carried out [34]. A SIMPLE algorithm was used to solve the pressure-velocity coupling. The velocity and the turbulent quantities were solved using second-order spatial discretization schemes. Instead, the volume fraction is solved using a first-order discretization scheme.

The computational domain of the simulations is a narrow axisymmetric slice of the vertical pipe, as showed in Fig. 2a and b. In the air-water models of the large pipe diameter cases ($D_{pipe} = 195\,mm$), the water flow enters in the bottom surface of the domain. Fully developed velocity profiles of water and gas were imposed, the volume fraction of the gas flow was imposed equal to 10^{-6}. The air flow inlet surface is located on the lateral surface of the domain, it has an axial extension of 6 mm, and it is located at 200 mm in the axial direction from the bottom face of the domain. The air velocity profile is assumed uniform and the size of the bubbles at the inlet was imposed constant, as reported in Table 2. In the steam-water cases, in order to be coherent with the results provided by Liao et al. [4], the inlet of both water and steam is located at the bottom face of the domain. The velocity profile of water is defined in fully developed conditions. Velocity and volume fraction profiles of steam are taken from the experimental measurements, reported in [4]. The steam is considered at the saturation temperature and the temperature profile of water is taken from the experiments. In all the other cases, H##, LB##e L###, the bottom surface of the domain is imposed as inlet of both liquid and gas phases. The profiles of velocity of water, velocity of gas and volume fraction are imposed as uniform and the respective values are reported in Table 2. In all the cases, the outlet boundary condition is defined on the top face of the domain, where a fixed pressure is imposed. At the wall, a no-slip boundary condition is imposed to both the continuous and the dispersed phases.

The computational mesh adopted to discretize all the cases is a structured grid (see Fig. 2c and d). The meshes used for the simulations performed with model A were built to have a dimensionless wall-distance y^+ greater than 30. This was necessary to use properly the wall functions associated to the standard $k-\varepsilon$ turbulence model. Instead, the meshes used for the simulations of models B and C, are characterized by a smaller thickness of the first layer near the wall. The value of y^+ was kept smaller than 1 in order to use the near-wall wall treatment used by the EB-RSM turbulence model. The mesh selected for the simulation of the large pipes air-water systems, providing grid-independent results, has 19550 cells, that one for the steam-water cases has 31250 cells. The meshes used for the small pipes H##, LB##e L### have, respectively, 16000, 13500, and 15000 cells.

4. Results and discussion

All the 18 cases listed in Table 2 were firstly simulated with the model A introduced in Section 2.5. Then models B and C were investigated in order to improve the performances especially with small pipe diameters. In the discussion, the CFD simulation results are compared both with experimental data available from the test

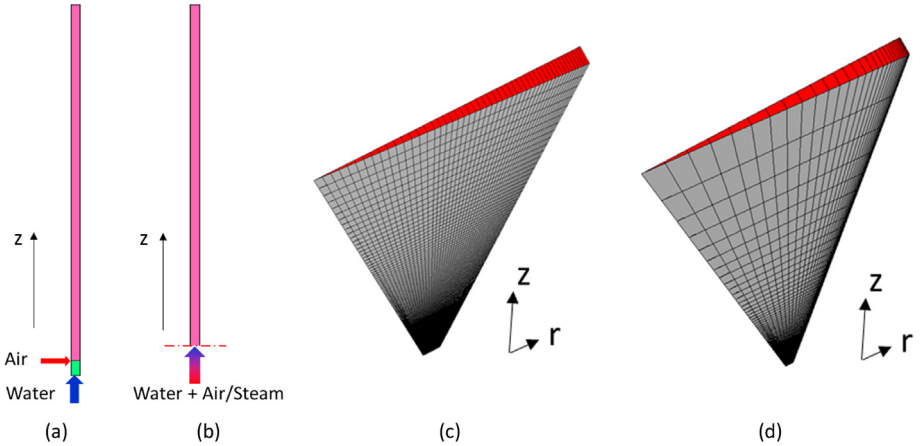

Fig. 2. Schematic of the computational domains and the meshes for the simulated cases. a) vertical section of the domain used for the air-water TOPFLOW cases; (b) vertical section of the domain used for all other cases; (c) mesh adopted for simulations with model A; (d) mesh adopted for simulations with models B and C.

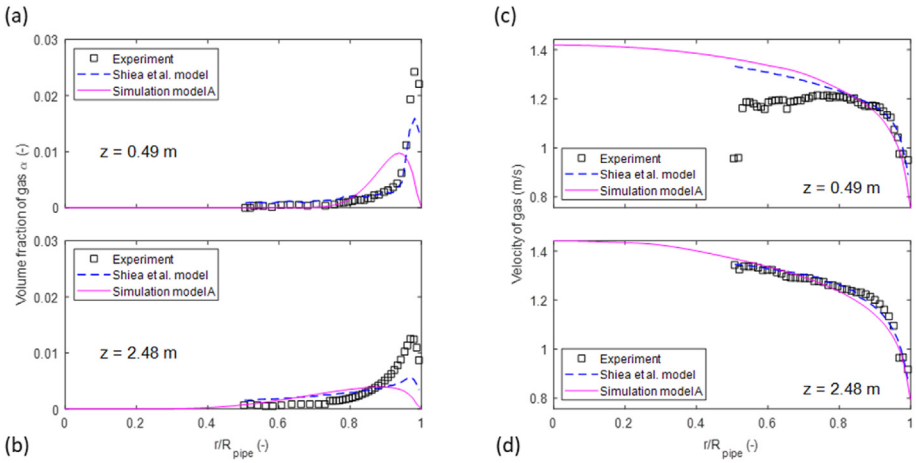

Fig. 3. Case 008: radial profiles of (a–b) volume fraction and (c–d) velocity of gas obtained by the experimental measurements (symbols), the model proposed by Shiea et al. (dashed lines), and model A (solid lines). Results are reported at two different distances from the air injection point: (a),(c) at z = 0.49 m and (b), (d) at z = 2.48 m.

campaign and with simulations results obtained from other researchers. For the TOPFLOW cases the results of the model III developed by Shiea et al. [2] is considered. For small pipes cases [31–33] the computational results presented by Colombo et al. [6] are used. The predictions obtained by Liao et al. [4] are used as a reference in the steam-water cases. Results are compared using radial profiles of physical quantities defined as a function of the dimensionless radius r/R, where the value 0 corresponds to the pipe centre, and the value 1 corresponds to the wall.

In the following sections, the radial profiles of the analysed quantities are reported for a reduced list of the entire experimental database. In order to show the results also for the cases not included in the reduced list, two different definitions of the error between experimental measurements and the simulated data were introduced:

$$Err\ (norm) = \frac{RMSD}{\overline{f_{EXP}}} = \frac{\sqrt{\frac{\sum_{i=1}^{N}\left(f_{CFD_i} - f_{EXP_i}\right)^2}{N}}}{\sqrt{\frac{\sum_{i=1}^{N}\left(f_{EXP_i}\right)^2}{N}}} = \frac{\sqrt{\sum_{i=1}^{N}\left(f_{CFD_i} - f_{EXP_i}\right)^2}}{\sqrt{\sum_{i=1}^{N}\left(f_{EXP_i}\right)^2}} \quad (33)$$

$$Err\ (Area) = \frac{\left|\int_0^{R_{pipe}} f_{CFD}dr - \int_0^{R_{pipe}} f_{EXP}dr\right|}{\left|\int_0^{R_{pipe}} f_{EXP}dr\right|} \quad (34)$$

The first one ("norm") is given in terms of Normalized Root Mean Square Deviation (RMSD) between the computed and experimental values at the *i* locations of the measurements. For the average of the experimental values at the denominator of Eq. (33), a 2-norm definition has been chosen. The second error ("Area") is defined as the relative error of the difference among the area subtended to the spatial profiles of the physical quantities f of interest (Eq. (34)). The integral for the experimental values, used also for the normalization, is done using the trapezoidal rule for the discrete measured values.

4.1. Model A results

Model A shows acceptable results only in the TOPFLOW cases in air-water systems. Results of cases 008 and 063 are reported in

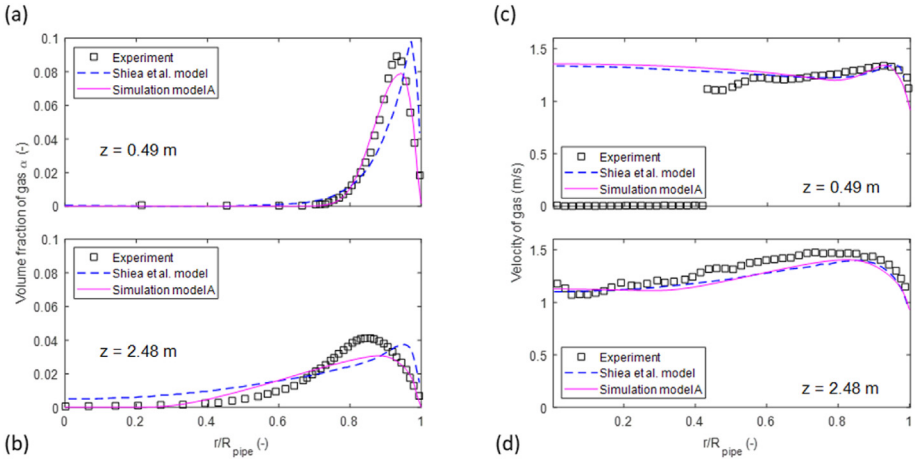

Fig. 4. Case 063: radial profiles of (a–b) volume fraction and (c–d) velocity of gas obtained by the experimental measurements (symbols), the model proposed by Shiea et al. (dashed lines), and model A (solid lines). Results are reported at two different distances from the air injection point: (a),(c) at z = 0.49 m, and (b),(d) at z = 2.48 m.

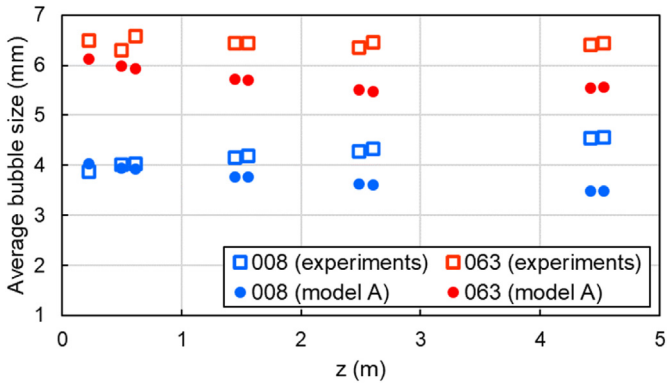

Fig. 5. Cases 008 and 063: evolution of the bubble size, averaged on the cross-section of the pipe, along the axial direction. Experimental measurements (open symbols) and results computed using model A (dots).

Figs. 3 and 4. The datasets of these experiments include radial profiles measured at different distance from the air inlet. Results in terms of profiles of volume fraction of gas and velocity of gas are showed at two different heights, 0.49 m and 2.48 m from the air injection point. The case 008 is characterized by a low superficial gas velocity and a very pronounced peak of the volume fraction of gas at the wall (see Fig. 3a). Model A is capable to identify a peak of volume fraction near the wall but its top value is largely underestimated and its width is overestimated. The relative errors computed using the norm and the subtended area of the computed and measured profiles are respectively equal to 85% and 7%. Also in the results obtained by the model proposed by Shiea et al. the height of the peak was underestimated, but the width and the position of the peak was better represented. Good agreement with both experimental and computed results by Shiea et al. is achieved in terms of radial profiles of the gas velocity, especially at higher distance from the inlet (see Fig. 3b). Case 063, shown in Fig. 4, is characterized by a much higher gas surface velocity at the same liquid surface velocity than case 008. In this case there is again a pronounced peak of the volume fraction near the wall near the air injection ($z = 0.49$ m in Fig. 4a), and then the bubbles spread liquid and the peak widens ($z = 2.48$ m in Fig. 4a). In the case 063 a very good agreement between measured and simulated data by the model A is reached, in terms of both volume fraction and gas velocity profiles. In the case 063 the relative errors are 23% (norm) and 4% (area), respectively, and both values are much lower than in the case 008. Compared to the results obtained by Shiea et al. the prediction of the location of the volume fraction peak is better reproduced in this work using model A.

To analyze how well the polydisperse modelling works, the evolution of the bubble size along the column axis is shown in Fig. 5. In both cases 008 and 063, the size of the bubbles is characterized by only a small variation along the axial direction. The bubble size predicted by simulations tends to decrease slowly in the axial direction, whereas experimental observations show a slight increase. This behaviour is caused by an overestimation of the breakage rate and turbulent dissipation rate, and the underprediction of the local gas volumetric fraction. However, the model generally agrees with the experimental data; the maximum errors in the bubble size for the cases 008 and 063 are −24% and −14%, respectively.

Among the other dataset analysed from the TOPFLOW database, consideration similar to those done for the case 008 can be also done for the case 042 (norm error 75%). Instead, simulations of the cases 028 and 072 reach a much better agreement with the

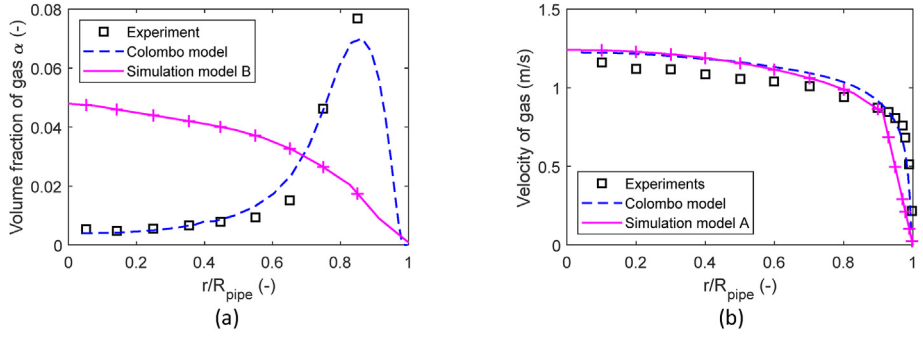

Fig. 6. Case H22: radial profiles of (a) volume fraction and (b) velocity of water, obtained by the experimental measurements (open symbols), the model proposed by Colombo et al. (dashed lines), and model A (solid lines).

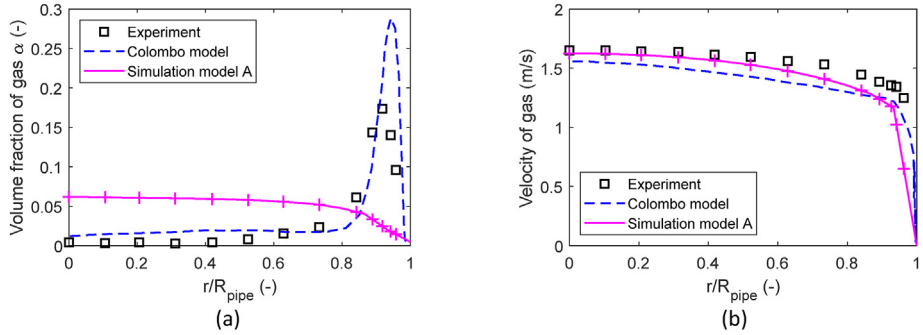

Fig. 7. Case LB30: radial profiles of (a) volume fraction and (b) velocity of gas obtained by the experimental measurements (open symbols), the model proposed by Colombo et al. (dashed lines), and model A (solid lines).

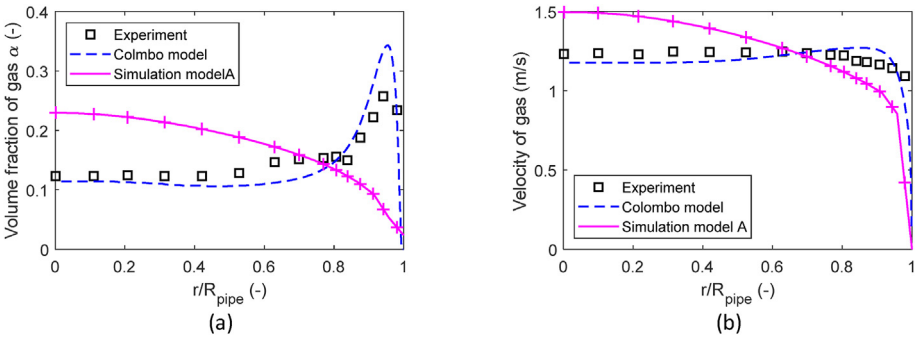

Fig. 8. Case L22A: radial profiles of (a) volume fraction and (b) velocity of water obtained by the experimental measurements (open symbols), the model proposed by Colombo et al. (dashed lines), and model A (solid lines).

experiments, with a norm error of 54% for the case 028 and 32% for the case 072.

In the experimental cases characterized by small pipe diameter, presented in Fig. 6, Fig. 7, and Fig. 8, the volume fraction profile is characterized by an high concentration of bubbles near the wall, as occurs in the tests with a large pipe. The main difference in the small diameter test cases is that the peak of the volume fraction remains very pronounced until the outlet, while the volume fraction in the centre of the pipes is not null, as observed in TOPFLOW experiments. In all these cases, the model A is not able to reproduce any peak of the volume fraction near the wall. This is evident observing Figs. 6a, 7a and 8a. The volume fraction profiles computed by the CFD simulations present a monotonic trend decreasing from the centreline of the pipe, where the volume fraction has its higher value, to the wall. This behaviour is inconsistent with the experimental measurements. The reason for the bad performances of model A in case of small pipes is probably related to the fact that a coarse computational grid is adopted near the wall, as needed in view of the requirement of having a wall y^+ greater than 30 to apply the Standard $k-\varepsilon$ model with wall functions. Moreover, the radial profiles of the lift and turbulent dispersion interfacial forces have very low mean values, around one order of magnitude lower than values computed using model B, presented in the next section. This kind of behaviour is observed not only in the three cases reported in Figs. 6, Figure 7, and Fig. 8, but in all the cases different to TOPFLOW. The error defined using the norm in small pipes cases ranges between 60% and 120%. All in all, the bad resolution of the grid at the wall, together with the adopted set of interfacial forces, results to be not suitable to simulate cases where the pipe diameter has a dimension comparable to the thickness of the first layer of the computational grid.

Analyzing the condensing steam-water flow experiments, the results are reported not only in terms of radial profiles, but also in terms of axial evolution of the volume fraction. In Fig. 9, the cross-section averaged volume fraction of steam is reported for the two experimental cases analysed here (118−1, 118−6). In both cases, the volume fraction computed by model A decreases too quickly, resulting in a large overestimation of the steam condensation. Note that the overprediction of the dissolution of bubbles is accentuated using the S-gamma poly-disperse modelling: in this case, the use of a monodispersed model allows computing a better representation of the axial evolution of the volume fraction, in line with the results provided by Liao et al. [4] (Fig. 9). The different effect given on the condensation by the two models can be better understood when looking at the computed diameter of the bubbles, reported in Fig. 10. In fact, the diameter of the bubbles computed by the polydisperse model drop to values of around 0.001 mm after less than 2 m from the inlet. This abrupt reduction results in an unphysical disappearance of the gas phase and, consequently, an overprediction of the condensation. Moreover Fig. 10 clarifies also the reason of the better predictions given by the monodisperse approach, since the mean bubble size measured experimentally does not change significantly over the column height.

The radial profiles of the steam volume fraction for the case 118−1 and 118−6 are reported in Figs. 11a and 12a, respectively. The peaks of bubble concentration near the wall are observable only in the region near the inlet (z = 0.608 m). Moving away from the inlet, the highlighted overestimation of condensation flattens the radial profiles of the steam volume fraction to very small values and no peaks are visible anymore. Similar considerations can be done for the gas velocity profiles, reported in Figs. 11b and 12b. The profiles computed using model A have a shape in line with the experiments, but the average velocity is significantly lower.

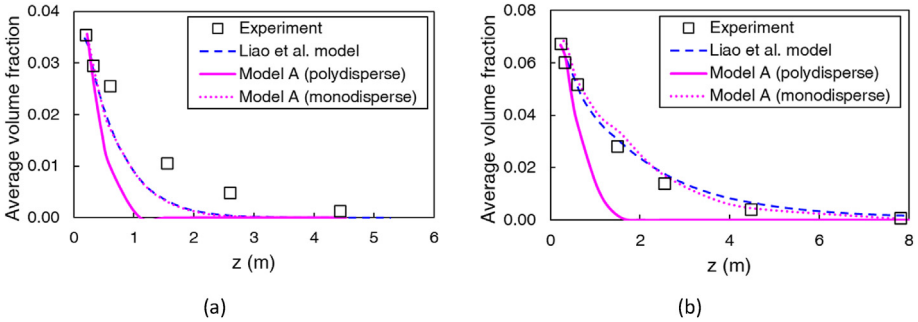

Fig. 9. Evolution of the volume fraction of gas, averaged on the cross-section of the pipe, along the axial direction for: (a) case 118−1, and (b) case 118−6. The results obtained using model A, with and without polydisperse modelling (solid and dotted lines, respectively), are compared with experimental data (open symbols) and results obtained by Liao et al. (dashed lines).

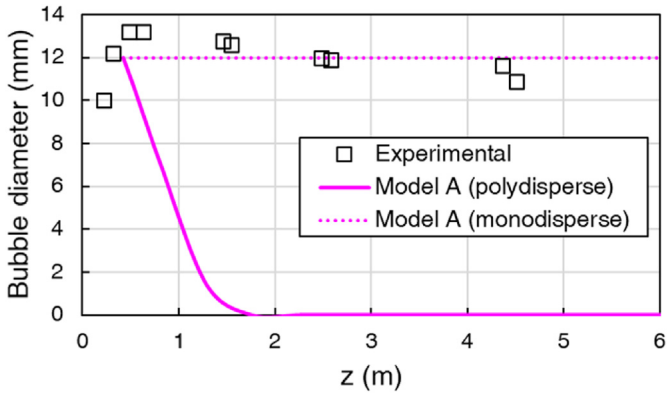

Fig. 10. Case 118–1: evolution of the Sauter mean diameter, averaged on the cross-section of the pipe, along the axial direction. Experimental data (open symbols), computed with the polydisperse model (solid line) and computed with the monodisperse model (dotted line).

4.2. Model B results

The rationale behind the formulation of Model B was the correct description of the sharp peaks of the volume fraction near the wall, that are typical of the small pipes system analysed in this paper. This model has been applied successfully to the cases with pipe diameter equal to 25 mm (H11, H12, H21, H22) and 38 mm (LB17, LB30, LB31). As reported in Figs. 13a and 14a, the accuracy of the computed results on the cases H22 and LB30 increases enormously with respect the profiles obtained by model A. With the introduction of the model B, the volume fraction of gas shows a peak near the wall, while it decreases to values near zero in the centre of the tube, as expected by experimental measurements. The position and the height of the peaks is quite well reproduced, and their accuracy is comparable to that obtained by the general model developed by Colombo and co-workers. The error defined using the norm (Eq. (33)) is reduced to values ranging between 25% and 42% (see Fig. 18 for more details). A good agreement between simulations and experiments is achieved also for the radial profiles of the velocity. The finer resolution of the computational grid near the wall allows a very good representation of the liquid and gas velocity profile decreases near the wall, see Figs. 13b and 14b. Note that in some cases the radial profiles of the velocity of liquid is reported (e.g. for the case H22), while in others the velocity of the gas is used (e.g. in the case LB30), according to the availability of experimental measurements. .

The results of the poly-disperse modelling of model B, are illustrated in Fig. 15. The evolution of the bubble size along the z-axis is compared with the measured values of the mean bubble size.

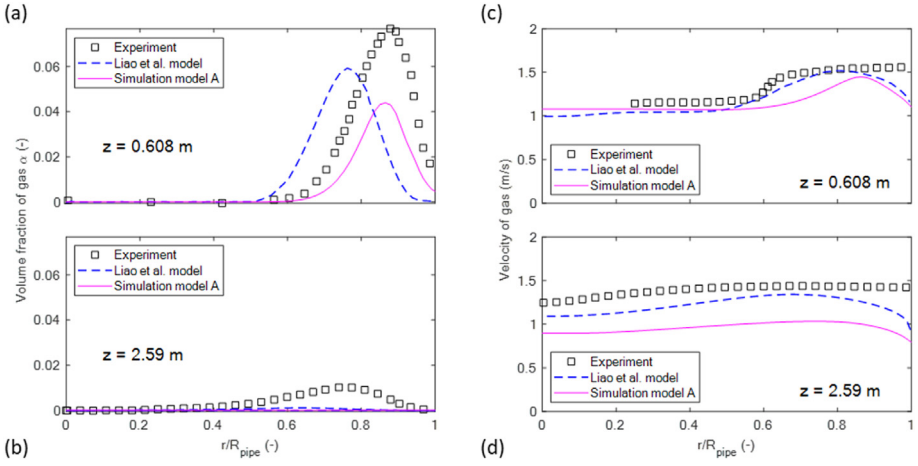

Fig. 11. Case 118–1: radial profiles of (a–b) volume fraction and (c–d) velocity of steam obtained by the experimental measurements (symbols), the model proposed by Liao et al. (dashed lines) and model A (solid lines). Results are reported at two different distances from the air injection point: (a), (c) at z = 0.608 m, and (b), (d) at z = 2.59 m.

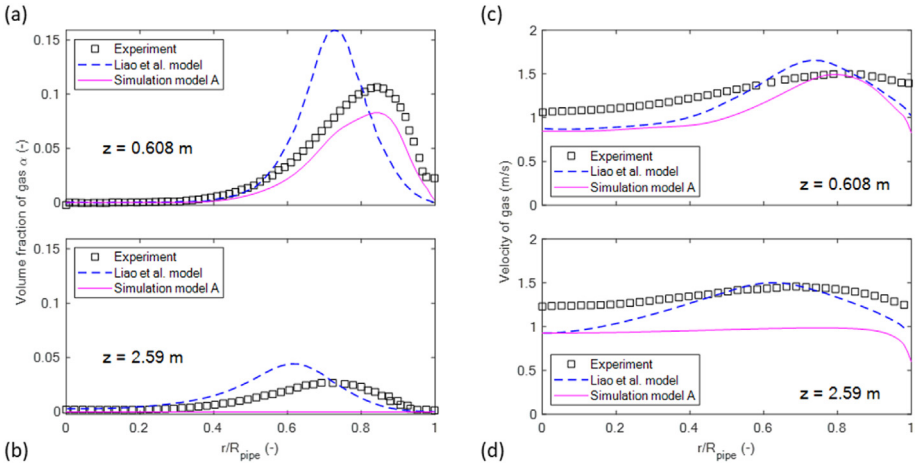

Fig. 12. Case 118–6: radial profiles of (a–b) volume fraction and (c–d) velocity of steam obtained by the experimental measurements (symbols), the model proposed by Liao et al. (dashed lines) and model A (solid lines). Results are reported at two different distances from the air injection point: (a), (c) at z = 0.608 m, (b), (d) at z = 2.59 m.

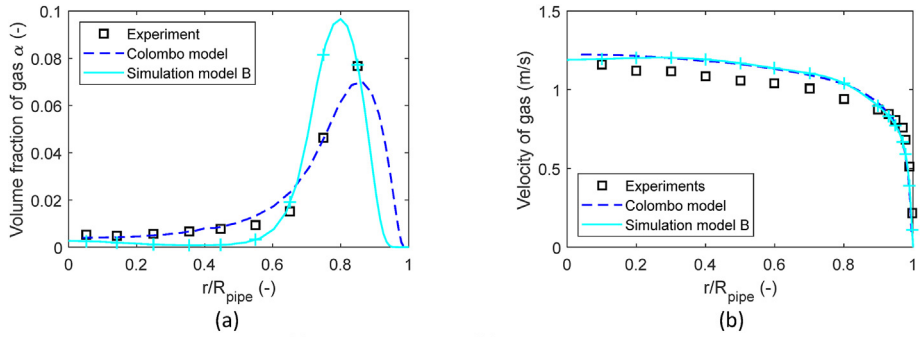

Fig. 13. *Case* H22: *radial profiles of (a) volume fraction and (b) velocity of* water *obtained by the experimental measurements (open symbols), the model proposed by Colombo* et al. *(dashed lines), and model B (solid lines).*

The bubble size predicted by model B shows good agreement with measurements especially for the case H22, where an almost constant values of the section-averaged bubble size is computed along the entire pipe. On the other hand, for the cases LB30 and L22A, the bubble size obtained by simulations is characterized by an approximately linear increase along the pipe. For the case H22 the predicted size is about 4% smaller than the measured one; for the cases LB30 and L22A, the predicted size is instead bigger than the measurements and the maximum errors are of +14% and +27%, respectively.

The simulation of the tests with large diameter pipes (TOPFLOW cases 008, 063, 042, 072, 028) using Model B was less successful than those of the tests on small-diameter cases, and for the sake of brevity the results are here omitted.

4.3. Model C results

Model C is a variation of the model B developed to improve the accuracy of the simulated results of the experimental database provided by Liu (cases L11A, L21C, L21B and L22A). In those cases, the diameter of the tube is equal to 57.2 mm and the model B is not able to predict the correct radial profile of the volume fraction. Analysing the results of the case L22A, showed in Fig. 16, the predictions obtained by model B show in fact an unphysical behaviour, and namely the computed radial profile for the volume fraction shows two peaks, one near the wall, as expected, and one near the mid-point of the radius. The computed effect is caused by the inversion of sign of the lift coefficient typical of the Tomiyama correlation. The adoption of a constant lift coefficient in Model C allows reaching a very good agreement between experiments and CFD simulations both in terms of void fraction and liquid velocity, as reported in Fig. 16. The top value of the peak of volume fraction of gas is slightly overestimated, but the shape of the profile is well

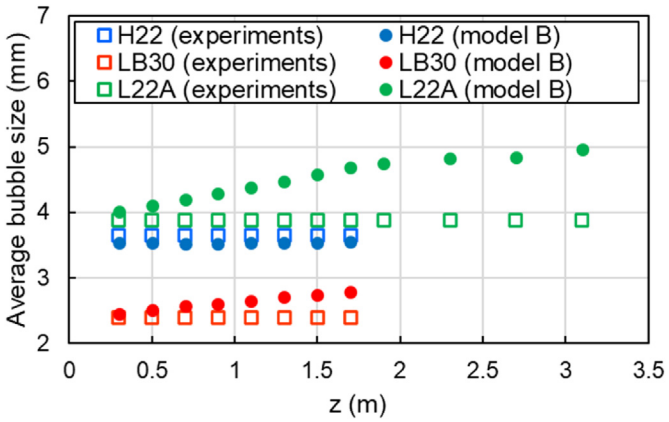

Fig. 15. Cases H22, LB30 and L22A: evolution of the bubble size, averaged on the cross-section of the pipe, along the axial direction. Experimental measurements (open symbols) and results computed using model B (dots).

reproduced. The accuracy of the results is similar to that obtained by Colombo and co-workers. A quantitative prove of the improvement of the accuracy can be obtained analysing the evolution of the error on the volume fraction profile of the case L22A moving from model A to model C. Using model A the error, defined using the norm, was 60%, then it was reduced to 45% introducing model B, and finally 38% adopting model C.

The simulation of the other cases using model C was less successful (see below for the detailed results).

The prediction of the bubble size evolution along the z-axis resulting from the poly-disperse modelling of model C are showed in Fig. 17. The results are very similar to those obtained by model B: the bubble size is well represented for case H22, and it increases

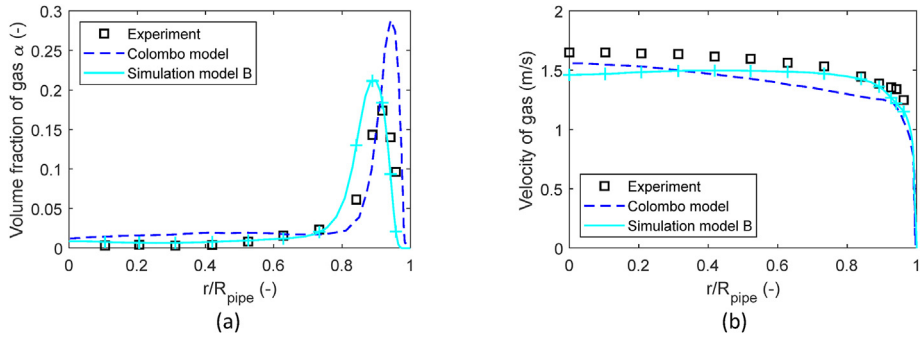

Fig. 14. Case LB30: radial profiles of (a) volume fraction and (b) velocity of water obtained by the experimental measurements (open symbols), the model proposed by Colombo et al. (dashed lines), and model B (solid lines).

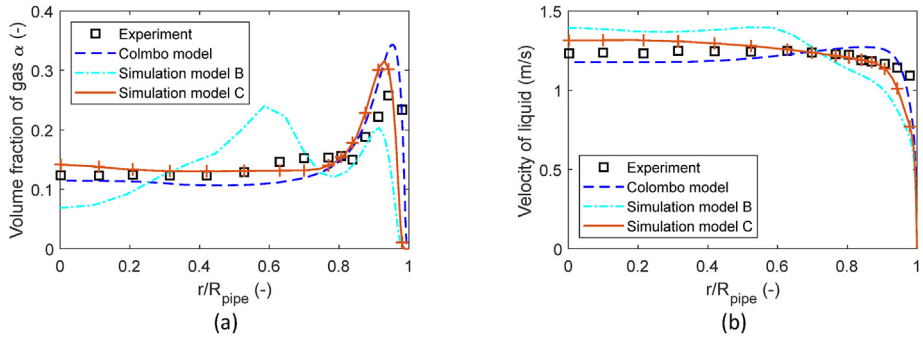

Fig. 16. Radial profiles of (a) volume fraction and (b) velocity of water of case L22A obtained by the experimental measurements, the model proposed by Colombo et al. and model C.

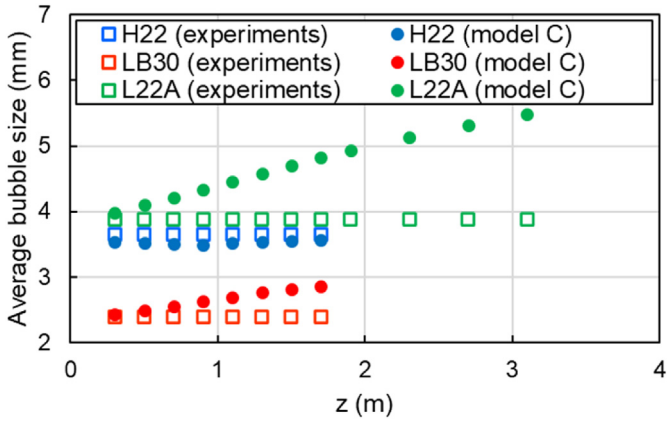

Fig. 17. Cases H22, LB30 and L22A: evolution of the bubble size, averaged on the cross-section of the pipe, along the axial direction. r Experimental measurements (open symbols) and results computed using model C (dots).

almost linearly for cases LB30 and L22A with an increment, computed at the measurement point, of +20% and +40%, respectively.

4.4. Summary of the results

In order to collect the results of the entire experimental dataset analysed here, two graphical representations are introduced. Fig. 18 summarizes of the entire experimental database in a plot reporting the diameter of the pipe in abscissa and the global gas hold-up in ordinate. The experimental cases are represented as circles the size of which is proportional to the average diameter of the bubbles inside the systems. Inside the plot, the regions where models A, B, and C are able to provide good accuracy are highlighted and also the main differences between the three models are reported. It is evident that no model was able to give decent predictions in all the cases: Model A was able to give good predictions for large diameter pipes, while for small diameters pipes Model B performed better, with Model C working better for slightly larger diameter pipes. It

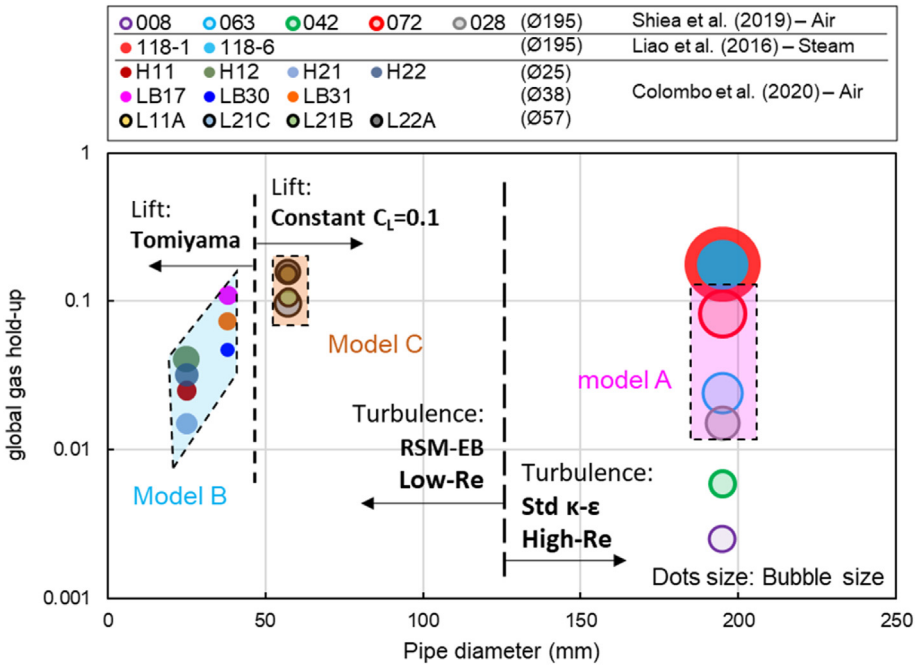

Fig. 18. Overview plot of all the experimental cases analysed in this paper with indication of the regions where each CFD model performs well and highlighting of the main differences between the models.

must be remarked that we do not have enough elements to say that a constant lift coefficient equal to 0.1 must be always used in case of pipes larger than 50 mm and smaller than 200 mm. However, we can reasonably say that the constant lift coefficient equal to 0.1 worked well for the investigated test cases.

A quantitative summary of the results is illustrated in Fig. 18 where all the relative errors between simulated and experimental radial profiles of volume fraction of gas are reported. In Fig. 18a the error computed using the norm definition (Eq. (33)) is shown, while in Fig. 18b the reported error is computed using the integral definition in Eq. (34). While it is clear that for the first 4 cases Model A wins over the others, and for the last 4 cases Model C is the best, the cases H* and LB* are better captured by Model B.

Note, that the simulation of the large diameter pipes, i.e. TOPFLOW cases 008, 063, 042, 072, 028 using Model B leads to volume fraction peaks near the wall that have an unphysical shape in all the analysed cases; in some cases, an oscillating shape with more than one peak was observed. The error values of the volume fraction profiles defined with norm and subtended area reached 100%. Moreover, in most cases, the CFD simulations diverged with high values of residuals and never reached a steady state condition (dashed bars in Fig. 18). In the cases of large diameter pipes the results obtained with Model C are similar of those obtained using model B: the errors reach 100% and most the CFD simulations diverge. The reason of such diverging behaviour seems to be the turbulence model, which results in unphysical values from the very beginning of the simulation. Similar problem could be solved by solving the transient problem until the steady state is reached. However, we decided to not modify the methodology applied here for those diverging simulations: all the results reported are obtained with a steady state solver. On the other hand, applying model C to cases with pipe diameter equal to 25 mm (H11, H12, H21, H22) and 38 mm (LB17, LB30, LB31), the simulations do not diverge but, in all cases, the errors are larger than those obtained using model B. The errors defined with norm and subtended area increase on average by 20% and 23%, respectively.

5. Conclusions

In this work the capability of three different Eulerian-Eulerian Two-phase models for reproducing the bubbly flow in vertical pipes was investigated using the commercial CFD code STAR-CCM+. A total of 18 different test cases having different pipe diameter and operating conditions was considered in the analysis. Three different models were considered, which rely on different interfacial forces and in the turbulence modelling, looking for the simplest one returning a good prediction for the largest set of the experimental data.

The results show that none from the investigated model can give decent predictions for all the investigated cases. However, a certain pattern can be recognized: for large diameter pipes (>15 cm) better results are obtained when the high-Reynolds standard k-epsilon is adopted, while for smaller diameter pipes a low-Reynolds approach based on Reynolds Stress Model works better for describing the volume fraction profiles at different height of the vertical pipe. Moreover, the analysis performed using the different models allowed highlighting that the lift force plays a crucial role in the description of the gas volume fraction profiles close to the walls: the results pointed out the suitability of the Tomiyama lift law for the simulation of pipes with small diameter, while a constant value of the lift coefficient allows to get good results in the simulations of pipes with intermediate diameter.

The results for the cases in which heat-transfer was considered, i.e., steam-water systems, showed that the population balance modelling here adopted is not capable of predicting of the proper condensation rates. However, this is not due to a methodology limitation, but rather due to a lack of suitable sub-models for describing bubble coalescence, breakage and, most importantly, shrinking due to condensation.

Declaration of competing interest

The authors declare that they have no known competing financial interests or personal relationships that could have appeared to influence the work reported in this paper.

Nomenclature

a_{ij}	Interaction area density (1/m)
α	Volume fraction
B	Birth term due to breakup of bubbles (1/s)
BSD	Bubble Size Distribution
C_D	Drag coefficient
C_L	Lift coefficient
$C_{p,i}$	Specific heat (J/kg/K)
C_{WL}	Wall lubrication coefficient
D	Death term due to breakup of bubbles (1/s)
D_{pipe}	Pipe diameter (m)
d_b	Bubble diameter (m)
d_{SM}	Sauter mean diameter (m)
E	Total energy (J/kg)
Eo	Eötvös number
Eo_d	Modified Eötvös number
F_{ij}^D	Drag force vector (N/m^3)
F_{ij}^L	Lift force vector (N/m^3)
F_{ij}^{TD}	Turbulent dispersion force vector (N/m^3)
F_{ij}^{WL}	Wall lubrication force vector (N/m^3)
g	Gravitational acceleration (m/s^2)
H	Total enthalpy (J/kg)
h	Specific enthalpy (J/kg)
h_c	Heat transfer coefficient between the continuous phase and the interface between phases ($W/m^2/K$)
Δh^{lat}	Specific latent heat (J/kg)
j_c	Superficial velocity of the continuous phase (m/s)
j_g	Superficial velocity of the dispersed phase (m/s)
k	Thermal conductivity (W/m/K)
k_c	Turbulent kinetic energy of the continuous phase (m^2/s^2)
k_{eff}	Effective thermal conductivity (W/m/K)
m	Mass transfer rate between phases ($kg/m^3/s$)
M	Interphase momentum transfer per unit volume ($kg/s^2/m^2$)
M_γ	γ order moment ($m^{\gamma-3}$)
μ_t	Turbulent viscosity (kg/m/s)
μ_{d_b}	Mean logarithmic of the particle diameter
$n(d_b)$	Bubble number density
n	Normal unit vector
n	Number of bubbles per unit volume
ν^t	Turbulent kinematic viscosity (m^2/s)
Nu	Nusselt number
n_w	Normal unit vector to the wall
p	Pressure (Pa)
$P(d_b)$	Probability density function of particle diameter
Pr	Prandtl number
Q	Heat transfer (W/m^3)
$Q_i^{(ij)}$	Heat transfer to phase i from the interface between phases i and j (W/m^3)
Re	Reynolds number
RST	Reynolds Stress Turbulence
ρ	Density (kg/m^3)

S_0	Zero-th order S_γ $(1/m^3)$
S_2	Second order S_γ $(1/m)$
s_{br}	Source term representing the effect of breakup
s_{cl}	Source term representing the effect of coalescence
σ	Surface tension (N/m)
$\sigma_{t,i}$	Turbulent Prandtl number
σ_α	Turbulent Prandtl number for the volume fraction of the dispersed phase
σ_{d_b}	Standard deviation of the particle diameter
s_m	Source term representing the effect of mass transfer between the phases
T	Molecular stress tensor $(kg/s^2/m)$
T^t	Turbulent stress tensor $(kg/s^2/m)$
T_{ij}	Temperature at the interface between phases i and j (K)
v	Velocity vector (m/s)
$v_{r,\|\|}$	Relative velocity component parallel to the wall (m/ s)
Wo	Wobble number
y	Wall distance of the gaseous phase (m)

Subscripts

c	Continuous phase
d	Dispersed phase
i	i-th phase
ij	Interaction between phases i and j
r	relative

References

[1] J. Feng, I.A. Bolotnov, Evaluation of bubble-induced turbulence using direct numerical simulation, Int. J. Multiphas. Flow 93 (Jul. 2017) 92–107, https://doi.org/10.1016/J.IJMULTIPHASEFLOW.2017.04.003.

[2] M. Shiea, A. Buffo, E. Baglietto, D. Lucas, M. Vanni, D. Marchisio, Evaluation of hydrodynamic closures for bubbly regime CFD simulations in developing pipe flow, Chemical Engineering \& Technology 42 (8) (2019) 1618–1626, https://doi.org/10.1002/ceat.201900116.

[3] Y. Liao, R. Rzehak, D. Lucas, E. Krepper, Baseline closure model for dispersed bubbly flow: bubble coalescence and breakup, Chemical Engineering Science 122 (Jan. 2015) 336–349, https://doi.org/10.1016/J.CES.2014.09.042.

[4] Y. Liao, D. Lucas, Poly-disperse simulation of condensing steam-water flow inside a large vertical pipe, International Journal of Thermal Sciences 104 (Jun. 2016) 194–207, https://doi.org/10.1016/J.IJTHERMALSCI.2016.01.016.

[5] M. Colombo, M. Fairweather, Multi-fluid computational fluid dynamic predictions of turbulent bubbly flows using an elliptic-blending Reynolds stress turbulence closure, Frontiers in Energy Research 8 (2020) 44, https://doi.org/10.3389/fenrg.2020.00044.

[6] M. Colombo, R. Rzehak, M. Fairweather, Y. Liao, D. Lucas, Benchmarking of computational fluid dynamic models for bubbly flows, Nuclear Engineering and Design 375 (2021), 111075, https://doi.org/10.1016/j.nucengdes.2021.111075.

[7] Software Siemens Digital Industries, Star-CCM+ User's Guide V. 16.02, 2021.

[8] M. Ishii, Thermo-fluid Dynamic Theory of Two-phase Flow, 1975 [Online], https://inis.iaea.org/search/search.aspx?orig_q=RN:7233706. (Accessed 1 December 2021).

[9] D. Ramkrishna, The framework of population balance, Population Balances (Jan. 2000) 7–45, https://doi.org/10.1016/B978-012576970-9/50003-5.

[10] A. Tomiyama, I. Kataoka, I. Zun, T. Sakaguchi, Drag coefficients of single bubbles under normal and micro gravity conditions, Jsme International Journal Series B-fluids and Thermal Engineering 41 (1998) 472–479.

[11] A. Tomiyama, H. Tamai, I. Zun, S. Hosokawa, Transverse migration of single bubbles in simple shear flows, Chemical Engineering Science 57 (11) (Jun. 2002) 1849–1858, https://doi.org/10.1016/S0009-2509(02)00085-4.

[12] R.M. Sugrue, A Robust Momentum Closure Approach for Multiphase Computational Fluid Dynamics Applications, PhD thesis, Department of Nuclear Science and Engineering, Massachusetts Institute of Technology, Cambridge, 2017.

[13] R.M. Wellek, A.K. Agrawal, A.H.P. Skelland, Shape of liquid drops moving in liquid media, Aiche Journal 12 (1966) 854–862.

[14] D. Shaver, M. Podowski, Modeling of interfacial forces for bubbly flows in subcooled boiling conditions, Transactions of the American Nuclear Society 113 (2015) 1368–1371.

[15] A.D. Burns, Th Frank, I.S. Hamill, J. Shi, The Favre Averaged Drag Model for Turbulent Dispersion in Eulerian Multi-phase Flows, 5th International Conference on Multiphase Flow, Yokohama, 2004.

[16] S.P. Antal, R.T. Lahey, J.E. Flaherty, Analysis of phase distribution in fully developed laminar bubbly two-phase flow, International Journal of Multiphase Flow 17 (5) (Sep. 1991) 635–652, https://doi.org/10.1016/0301-9322(91)90029-3.

[17] R. Rzehak, E. Krepper, CFD modeling of bubble-induced turbulence, International Journal of Multiphase Flow 55 (Oct. 2013) 138–155, https://doi.org/10.1016/J.IJMULTIPHASEFLOW.2013.04.007.

[18] S. Lo, D. Zhang, Modelling of break-up and coalescence in bubbly two-phase flows, The Journal of Computational Multiphase Flows 1 (1) (Jan. 2009) 23–38, https://doi.org/10.1260/175748209787387106.

[19] D.P. Hill, The Computer Simulation of Dispersed Two-phase Flow, PhD thesis, Department of Mechanics, Imperial College of Science, Technology and Medicine, London, 1998.

[20] C. Tsouris, L.L. Tavlarides, Breakage and coalescence models for drops in turbulent dispersions, Aiche Journal 40 (1994) 395–406.

[21] C.A. Coulaloglou, L.L. Tavlarides, Description of interaction processes in agitated liquid-liquid dispersions, Chemical engineering science 32 (11) (1977) 1289–1297.

[22] W. Yao, C. Morel, Volumetric interfacial area prediction in upward bubbly two-phase flow, International journal of heat and mass transfer 47 (2) (2004) 307–328.

[23] V.G. Levich, Physicochemical Hydrodynamics, Prentice-Hall, Englewood Cliffs, N.J., 1962.

[24] L.I. Zaichik, O. Simonin, V.M. Alipchenkov, Turbulent collision rates of arbitrary-density particles, International journal of heat and mass transfer 53 (9) (2010) 1613–1620.

[25] H. Luo, Coalescence, Breakup and Liquid Circulation in Bubble Column Reactors, Ph.D. Thesis, Norges Tekniske Hoegskole, Trondheim, 1993.

[26] A. Tomiyama, Progress in computational bubble dynamics, in: 7th Workshop on Multiphase Flow, vol. 27, May, 2009.

[27] W.P. Jones, B.E. Launder, The prediction of laminarization with a two-equation model of turbulence, International Journal of Heat and Mass Transfer 15 (2) (Feb. 1972) 301–314, https://doi.org/10.1016/0017-9310(72)90076-2.

[28] S. Lardeau, R. Manceau, Computations of complex flow configurations using a modified elliptic-blending Reynolds-Stress model, in: 10th International ERCOFTAC Symposium on Engineering Turbulence Modelling and Measurements, Marbella, Spain, 2014.

[29] S. Hosokawa, A. Tomiyama, S. Misaki, T. Hamada, Lateral Migration of Single Bubbles Due to the Presence of Wall, Nov. 2002, https://doi.org/10.1115/FEDSM2002-31148.

[30] M. Beyer, D. Lucas, J. Kussin, P. Schütz, Air-water Experiments in a Vertical DN200-Pipe, 2008.

[31] S. Hosokawa, A. Tomiyama, Multi-fluid simulation of turbulent bubbly pipe flows, Chemical Engineering Science 64 (24) (Dec. 2009) 5308–5318, https://doi.org/10.1016/J.CES.2009.09.017.

[32] T.J. Liu, S.G. Bankoff, Structure of air-water bubbly flow in a vertical pipe—II. Void fraction, bubble velocity and bubble size distribution, International Journal of Heat and Mass Transfer 36 (4) (Mar. 1993) 1061–1072, https://doi.org/10.1016/S0017-9310(05)80290-X.

[33] T.J. Liu, The role of bubble size on liquid phase turbulent structure in two-phase bubbly flow, in: Proc. Third International Congress on Multiphase Flow ICMF, vol. 98, 1998, pp. 8–12.

[34] S.v. Patankar, D.B. Spalding, A calculation procedure for heat, mass and momentum transfer in three-dimensional parabolic flows, International Journal of Heat and Mass Transfer 15 (10) (Oct. 1972) 1787–1806, https://doi.org/10.1016/0017-9310(72)90054-3.